




Inhomogeneous excitation-regulated coherent strain wave in $2H\text{-MoTe}_2$ revealed by ultrafast electron microscopy

Yongzhao Zhang ^{1,2,3}, Shuaishuai Sun ¹, Wentao Wang,^{1,3} Huanfang Tian,¹
Jianqi Li,^{1,3,4,*} Jun Li,^{1,†} and Huaixin Yang ^{1,3,5,‡}

¹*Beijing National Laboratory for Condensed Matter Physics, Institute of Physics, Chinese Academy of Sciences, Beijing, 100190, People's Republic of China*

²*Institute of Quantum Materials and Physics, Henan Academy of Science, Zhengzhou 450046, People's Republic of China*

³*School of Physical Sciences, University of Chinese Academy of Science, Beijing, 100190, People's Republic of China*

⁴*Songshan Lake Materials Laboratory, Dongguan, Guangdong, 523808, People's Republic of China*

⁵*Yangtze River Delta Physics Research Center Co., Ltd., Liyang, Jiangsu, 213300, People's Republic of China*



(Received 19 July 2023; revised 28 November 2023; accepted 29 November 2023; published 27 December 2023)

The field of optical detection and manipulation of transient states with ultrafast lasers is rapidly growing and shows great promise. In this field, new states can be generated through photodoping or optical-induced strain. However, traditional ultrafast measurements have been plagued by the challenge of inhomogeneous excitation, which is difficult to avoid. Nevertheless, recent developments suggest that this situation might change and open up more possibilities for the ultrafast manipulation of materials. One such possibility involves introducing nonuniform order parameter fields, like carrier density gradients. In this study, we demonstrate the potential to manipulate the coherent photoacoustic wave in $2H\text{-MoTe}_2$ by adjusting the homogeneity of laser excitation, which is closely linked to the thickness of the flake. Our ultrafast electron diffraction experiments reveal that, as the flake thickness increases, the photoacoustic wave transforms from a standing wave with breathing motions to a solitonlike traveling wave. This transformation is characterized by distinct diffraction intensity oscillations. For flake thicknesses below the critical value of approximately 40 nm, homogeneous excitation results in out of phase intensity oscillations of the Friedel pairs, and only a fundamental frequency component is detected. On the other hand, in thicker flakes, inhomogeneous excitation leads to in-phase intensity oscillations and the emergence of a second harmonic component. Overall, our findings highlight the unique aspects of inhomogeneous excitation and its implications for the optical control of exotic properties in strain-related transient states.

DOI: [10.1103/PhysRevB.108.245426](https://doi.org/10.1103/PhysRevB.108.245426)

I. INTRODUCTION

Ultrafast measurements with weak perturbations have provided valuable tools for characterizing the intrinsic properties of materials and disentangling complex degrees of freedom in the time domain [1,2]. Typically, these measurements require uniform excitation in the three-dimensional profile of the probe beam. However, a widespread challenge arises from the penetration depth mismatch [3,4] between the pump and probe beams in optical-pump and electron-, THz-, or x-ray-probe schemes. This mismatch often necessitates sophisticated simulations [5,6] for result interpretation, even with special designs such as grazing incidence [7] or the use of very thin films [8].

On the other hand, ultrafast strong excitations have emerged as novel techniques for manipulating and controlling the physical properties of quantum materials through photoinduced doping, strain, or Floquet engineering [9,10]. Recently, a novel ordered state was discovered in a charge density wave (CDW) system using nonuniform ultrafast laser

excitation, resulting in the creation of macroscopic domain walls separating normal and inverted CDW regions [11]. These domain walls may even exhibit superconductivity [12]. Inhomogeneous excitation presents an avenue for ultrafast material control through strain or domain manipulation.

Coherent phonons generated by optical excitation have been extensively studied for their potential application in changing or manipulating the fascinating properties [13–15] of low-dimensional electronic materials, which is of significant importance for accelerating the functionalization of two-dimensional materials in electronic device applications [16], and detecting coherent phonons has gradually matured with the development of various ultrafast experimental methods, including spectroscopic techniques [17,18], x-ray diffraction [19], and transmission electron microscopy [20–22]. Previous studies have elaborated on the generation mechanisms, such as deformation potential and thermoelasticity, of both coherent optical phonons (COPs) and coherent acoustic phonons (CAPs) [23,24]. In the context of CAPs, homogeneous optical excitation is typically observed when the penetration depth of the pump beam exceeds the sample thickness [25–27]. Conversely, inhomogeneous excitation often occurs in samples with thicknesses much greater than the optical penetration depth [28]. Both excitation methods can be utilized to manipulate the coherent strain wave.

*ljq@iphy.ac.cn

†junli@iphy.ac.cn

‡hxyang@iphy.ac.cn

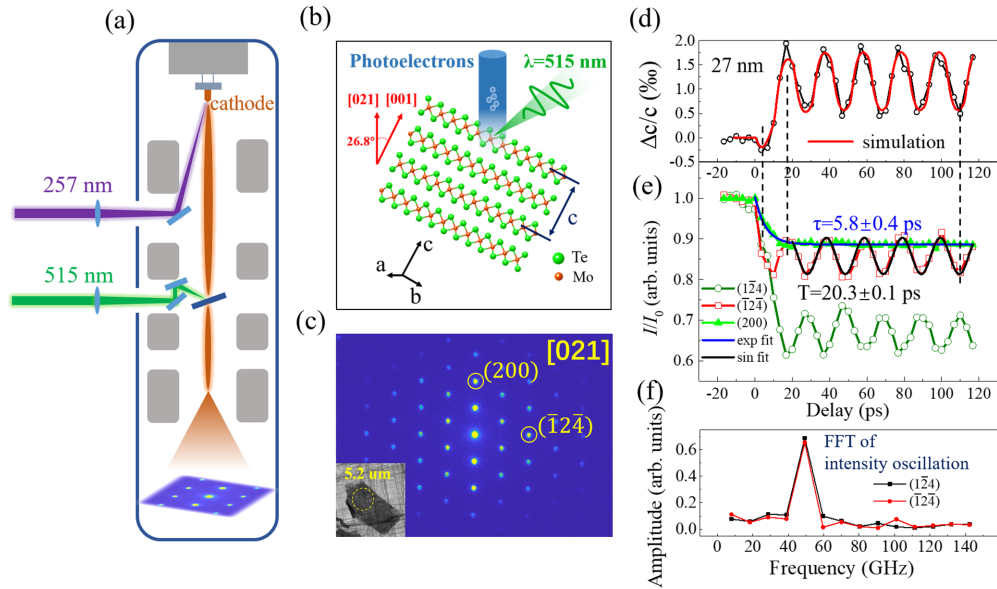


FIG. 1. Schematic of the time-resolved experiment and signals of the measured transients in 27 nm $2H$ - MoTe_2 film. (a) Schematic of UTEM. (b) Experimental setup. The dimension of the pump laser is $50 \times 60 \mu\text{m}$ (FWHM) with $11 \text{ mJ}/\text{cm}^2$ fluence. (c) Diffraction pattern along the $[021]$ zone axis. (d) Fast contraction and relaxation of lattice constant c . Red line: simulation of atomic displacement by solving wave equation. (e) Temporal response of Bragg peaks $(\bar{1}\bar{2}4)$, $(\bar{1}2\bar{4})$, and (200) . The intensity drop of (200) caused by the Debye-Waller effect is fitted by an exponential function with time constant $\tau = 5.8 \text{ ps}$. The period of intensity oscillation in $(\bar{1}\bar{2}4)$ and $(\bar{1}2\bar{4})$ determined by sinusoidal fitting is $20.3 \pm 0.1 \text{ ps}$. (f) Fast Fourier transformation of intensity oscillation.

In the field of ultrafast transmission electron microscopy (UTEM), several techniques with high spatial and temporal resolution, including selected-area electron diffraction (SAED) [29,30], bright (or dark) field imaging [31,32], and convergent-beam diffraction (CBED) [33,34], have proven to be powerful tools for detecting strain waves due to their high sensitivity to lattice order and crystal orientation. In this study, we focus on a $2H$ - MoTe_2 film, which remains relatively stable under ambient conditions. However, under excess Te deficiency, electric field, strain, or laser excitation, it can transform into the $1T'$ phase due to the extremely low-energy barrier with $1T'$ - MoTe_2 [35,36]. Recently, an electric field induced transient state between the semiconducting $2H$ phase and the metallic $1T'$ phase was reported [37]. This polymorphism greatly benefits electronic applications in oscillators and sensors [38,39]. In this work, we employ ultrafast SAED to investigate the dynamics of laser-induced longitudinal acoustic phonons in the $2H$ - MoTe_2 film. Our experimental and simulation results demonstrate that the inhomogeneous laser excitation can induce the second harmonic component of the strain wave. The observed acoustic phonons and their modulation of atomic rearrangement contribute to a refined understanding of the dynamical response of $2H$ - MoTe_2 under photoexcitation.

II. METHODS

Figure 1(a) illustrates the schematic of UTEM based on the pump-probe technique. The probe laser is generated by frequency quadrupling a 257 nm laser and the pump laser is generated by frequency doubling a 515 nm laser, both derived from a fundamental laser beam (1030 nm, 190 fs). A multilayer $2H$ - MoTe_2 film is obtained through mechanical

exfoliation from a bulk crystal and subsequently transferred onto a carbon nanotube substrate. To capture out of plane information, the sample is tilted by 26.8° around the $[100]$ direction, aligning the incident photoelectron beam parallel to the $[021]$ zone axis of the crystal, as depicted in Fig. 1(b). Under this configuration, the angle between the pump laser and the sample surface is 50.5° .

The probing area has a diameter of $5.2 \mu\text{m}$ [see inset of Fig. 1(c)], while the pump laser has a size of $50 \times 60 \mu\text{m}$ [full width at half maximum (FWHM)]. The fluence of the pump laser is set to $11 \text{ mJ}/\text{cm}^2$ for the 27 nm sample and $4.4 \text{ mJ}/\text{cm}^2$ for the 63 nm sample. The determination of the sample thickness is based on the acoustic wave velocity and the detected oscillation period of the fundamental mode, which is further discussed in the main text, and is supported by electron energy loss spectroscopy (EELS) measurements (see Supplemental Material, Sec. 1 [40]; also see Refs. [41–45]). All ultrafast SAED measurements were carried out at room temperature (300 K) with a laser repetition rate of 33 kHz. By adjusting the time delay, a series of structural evolutions under nonequilibrium conditions were captured within a time window of 120 ps. $2H$ - MoTe_2 possesses a hexagonal structure with space group $P6_3/mmc$ and a honeycomblike in-plane structure [46] (refer to Fig. S2(a) in the Supplemental Material [40]). Moreover, $2H$ - MoTe_2 is an indirect band gap semiconductor with a band gap of 0.9 eV [47]. However, when thinned down to a monolayer, it undergoes a transition to a direct band gap semiconductor with a band gap of 1.1 eV [48].

III. RESULTS AND DISCUSSION

The UTEM setup and experimental schematic are presented in Figs. 1(a) and 1(b), respectively. For a more detailed

description of the experimental methods, please refer to the Methods section. Figure 1(c) displays a typical SAED pattern of $2H\text{-MoTe}_2$ generated by photoelectrons at a negative time delay. The inset of Fig. 1(c) depicts the transmission electron microscopy (TEM) image of the exfoliated $2H\text{-MoTe}_2$ sample with a thickness of 27 nm. The oscillation of the lattice constant c , as shown in Fig. 1(d), indicates the presence of out of plane longitudinal acoustic phonons (breathing mode) in the film following laser excitation. This breathing mode is confirmed by the intensity variation of an in-plane peak (200) in Fig. 1(e), which exhibits a drop in intensity caused by the Debye-Waller effect [49] with a time constant of $\tau = 5.8$ ps. To gain further insight, we conducted time-resolved electron diffraction measurements along the [001] zone axis using the same experimental setup. However, no significant intensity oscillations were observed (see Supplemental Fig. S2(b) [40]).

We now focus on investigating the generation mechanism of CAPs in our experiment. In semiconductors, CAPs can be generated through thermoelasticity, deformation potential, and inverse piezoelectric processes following laser excitation [23]. In the case of $2H\text{-MoTe}_2$, the absence of a piezoelectric response can simplify the photoinduced strain generation due to its centrosymmetric structure. The distribution of electrons and lattice temperature can be altered by the generation, redistribution, and recombination of photogenerated carriers, leading to changes in interatomic forces and a new equilibrium atomic position. Consequently, the lattice either expands or contracts toward this new equilibrium position, and due to overshoot, the atoms undergo periodic oscillations akin to resonators.

The deformation potential parameter along the c direction of $2H\text{-MoTe}_2$ is approximately $-1.12 \times 10^{-24} C_{33}$ J [50] (C_{33} represents Young's modulus). This value suggests that carriers induce lattice contraction, while thermoelasticity causes lattice expansion. Thus, the lattice constant c exhibits rapid contraction during the time interval of 0–3.7 ps, followed by expansion toward the new equilibrium position [Fig. 1(d)]. The red line in Fig. 1(d) represents the simulation results obtained by solving the wave equation (3) considering thermoelasticity and deformation potential. Further details about the calculation can be found in the following discussion and Sec. S6 of the Supplemental Material [40].

Figure 1(e) illustrates the intensity oscillation of out of plane Friedel pairs, which exhibit an out of phase characteristic. This behavior has been extensively reported and can be effectively described by the geometrical theory of diffraction [29,32,51]. The sinusoidal fitting of the intensity oscillation and the corresponding fast Fourier transform (FFT) results reveal a period of 20.3 ps, corresponding to a frequency of 49.3 GHz. The linear chain model has been shown to accurately describe out of plane acoustic phonons in van der Waals materials [52], providing a simple dispersion relation between frequency (f) and wavenumber k

$$f = \frac{1}{\pi} \sqrt{\frac{K}{\mu}} \sin\left(\frac{kd_z}{2}\right), \quad (1)$$

where μ , d_z , and K are the mass per unit area, out of plane periodicity of the layers, and the interlayer elastic constant per unit area, respectively. The long wavelength limit (or

continuous medium) provides $f = \sqrt{\frac{K}{\mu}} \frac{kd_z}{2\pi} = \frac{v}{\lambda}$. Thus, the wave velocity

$$v = \sqrt{\frac{K}{\mu}} d_z = \sqrt{\frac{C_{33}}{\rho}}. \quad (2)$$

The out of plane longitudinal elastic modulus (C_{33}) of $2H\text{-MoTe}_2$ is reported to be 54 GPa [53], and its density (ρ) is 7.7 g/cm³, resulting in a longitudinal acoustic wave velocity (v) of 2.65 km/s. The period of acoustic wave in the free-standing film can be determined using the relationship $T = \frac{2d}{v}$, where d represents the sample thickness. Thus, based on the measured period of the acoustic wave, the sample thickness is estimated to be 27 nm.

In contrast, the ultrafast response of a 63 nm film exhibits more complex characteristics. Following laser excitation, both the in-plane and out of plane peaks display oscillations. Figure 2(a) presents the intensity oscillation of partial spots, and the corresponding FFT in Fig. 2(b) indicates the excitation of two vibration modes with a frequency ratio of 1:2. To fit the intensity, we employ a combination of sine functions with periods of T and $T/2$ [$\frac{I}{I_0} = \sum_{k=1}^2 a_k \sin(\frac{2\pi k}{T}t + \varphi_k)$]. The well-fitted results are depicted as blue curves in Fig. 2(a), which yield a vibration period (T) of 47.6 ± 0.5 ps and the corresponding frequency (f) of 21 ± 0.2 GHz.

We performed further analysis of the phases associated with the two frequencies and presented them in Fig. 2(c). Remarkably, the phases exhibit distinct characteristics in the Friedel pairs. The 21 GHz components predominantly display an out of phase characteristic, whereas the 42 GHz components show dominant in-phase oscillations. Additionally, concerning the 42 GHz components, there is a difference in the oscillation phase between the in-plane and out of plane peaks. For peaks with indices ($h00$), the oscillation phase is approximately zero, whereas for peaks with indices (hkl), where $l \neq 0$, the phase is π . These symmetrical or anti-symmetrical characteristics distributed on both sides of the direction [100] are visually evident in the two-dimensional phase mapping in reciprocal space depicted in Figs. 2(d) and 2(e). Previous observations of intensity oscillations in electron diffraction [32,54] were attributed to small zone-axis tilts resulting from shear or breathing modes. However, these explanations cannot account for the in-phase oscillations observed in Figs. 2(c) and 2(e).

It is worth mentioning that for peaks with indices ($hk0$), the diffraction amplitude remains unchanged for the longitudinal wave propagating along the c direction within the framework of kinematical theory. Thus, only Debye-Waller effect can be observed in Bragg peaks ($hk0$) obtained along the [001] direction (refer to the Supplemental Material [40], Fig. S2). As labeled in Fig. 2(d), all the diffraction peaks after No. 10 locate on the $a^* - b^*$ plane and can be indexed as ($h00$). These in-plane peaks ($h00$) and even (000) all show oscillation behavior (Fig. 2 and Fig. S3 in Supplemental Material [40]) when the sample is tilted to the [021] zone axis, whose phase is opposite to that of the out of plane points. This phenomenon indicates that the dynamic diffraction effect should be taken into consideration for these peaks. For example, in the multislice method simulation, the intensity of the incident

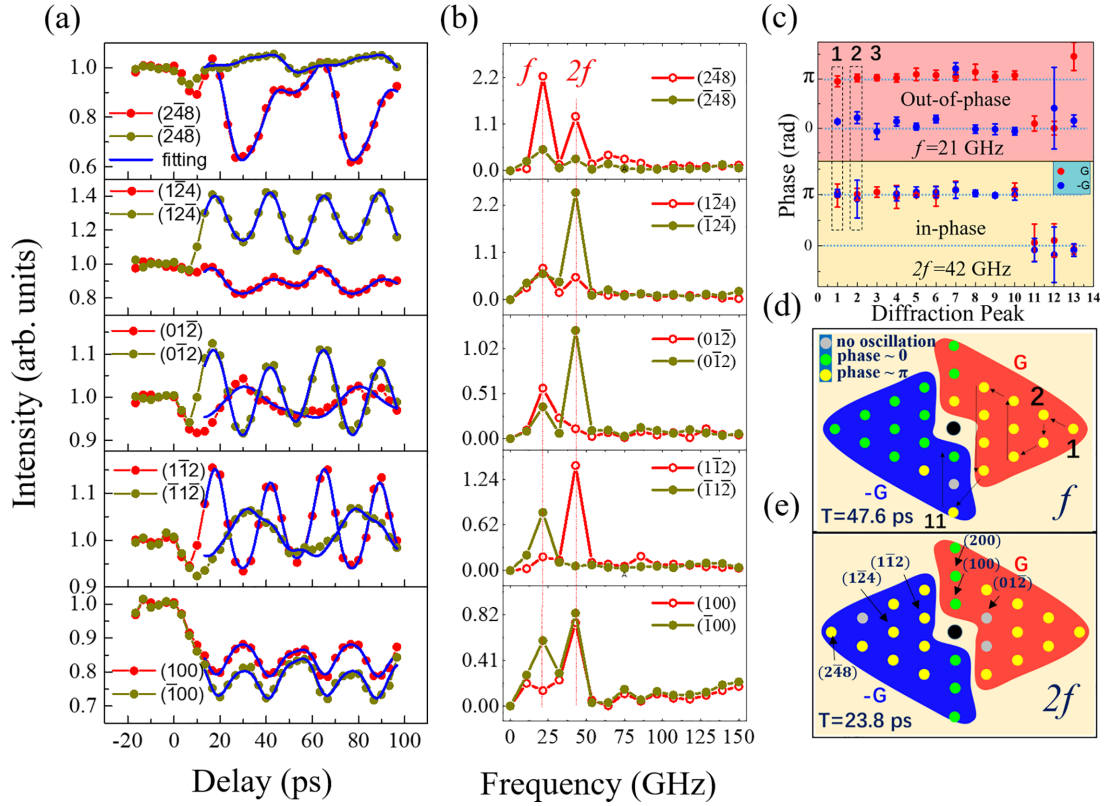


FIG. 2. Intensity oscillation of Friedel pairs in $2H$ -MoTe $_2$ with 63 nm thickness. (a) Time dependence of diffraction intensity of ten typical spots obtained along the $[021]$ zone axis. The blue curves represent the fitting results of the function $\frac{I}{I_0} = \sum_{k=1}^2 a_k \sin(\frac{2\pi k}{T}t + \varphi_k)$; each sinusoidal function describes a different oscillation frequency. (b) Fast Fourier transformation (FFT) amplitude of intensity oscillation in (a). Two dominant frequencies exist in the oscillation, corresponding to f and $2f$, respectively; $f = 21$ GHz. (c) Phases of the f and $2f$ components of the Friedel pairs. Axis x represents the number assigned to each diffraction peak shown in (d). Friedel pairs show different features in two different frequencies. Pink region: out of phase oscillation of Friedel pairs with frequency of 21 GHz (out of phase). Yellow region: in-phase oscillation of Friedel pairs with frequency of 42 GHz (in phase). The peaks (hkl) with $l \neq 0$ and $l = 0$ have inverted tendency for 42 GHz. (d,e) show the phase mapping in reciprocal space.

beam of a slice is always affected by the scattering process that happened in the former slice. Thus, the intensity oscillations of out of plane peaks would lead to the oscillation of in-plane peaks, including the central beam, and normally the intensity changes are opposite for the two types of diffraction peak, evidenced by the π phase jump observed in the lower panel in Fig. 2(c).

IV. ATOMIC DISPLACEMENT UNDER LASER EXCITATION

To obtain the layer motion μ induced by coherent phonons, the $2H$ -MoTe $_2$ film is treated as a continuous elastic medium. The one-dimensional (1D) elastodynamic wave equation can be described as follows:

$$\rho \frac{\partial^2 \mu}{\partial t^2} = C_{ij} \frac{\partial^2 \mu}{\partial z^2} + \lambda \frac{\partial \mu}{\partial t} + \frac{\partial \sigma_{\text{ext}}}{\partial z}, \quad (3)$$

where C_{ij} , λ , and ρ represent the components of the elastic moduli matrix, damping constant, and density, respectively. Components C_{33} and C_{44} correspond to the breathing and shear modes, respectively. Depth z is along the normal direction of the surface. σ_{ext} is the photoinduced stress term that is mainly composed of thermoelasticity σ_T and deformation

potential σ_e . Positive values of $\frac{\partial \sigma_{\text{ext}}}{\partial z}$ correspond to expansion of the lattice. In general,

$$\begin{aligned} \sigma_{\text{ext}} &= \sigma_T(z, t) + \sigma_e(z, t), \\ \sigma_T(z, t) &= -C_{ij} \beta [T(z, t) - T(z, 0)], \\ \sigma_e(z, t) &= -d_e n(z, t). \end{aligned} \quad (4)$$

The simulation utilizes coefficients β and d_e , representing the linear expansion coefficient and deformation potential, respectively. The specific values of these coefficients used in the simulation can be found in Supplemental Table S1 [40], and the time-dependent variation of σ_{ext} is detailed in Supplemental Sec. S6 [40]. The lattice temperature $T(z, t)$ and carrier density $n(z, t)$ are functions of depth z and time delay t , and their profiles may exhibit inhomogeneity along the depth direction due to the limited optical penetration depth.

Typically, when light interacts with a semiconductor with a band gap E_g (approximately 0.9 eV in the case of $2H$ -MoTe $_2$), electron-hole pairs are initially excited with excess energy of $h\nu - E_g$. This excess energy can be released to the lattice through nonradiative recombination of carriers [55,56]. The rising lattice temperature induced by electron-phonon coupling is described by a two-temperature model. The intensity

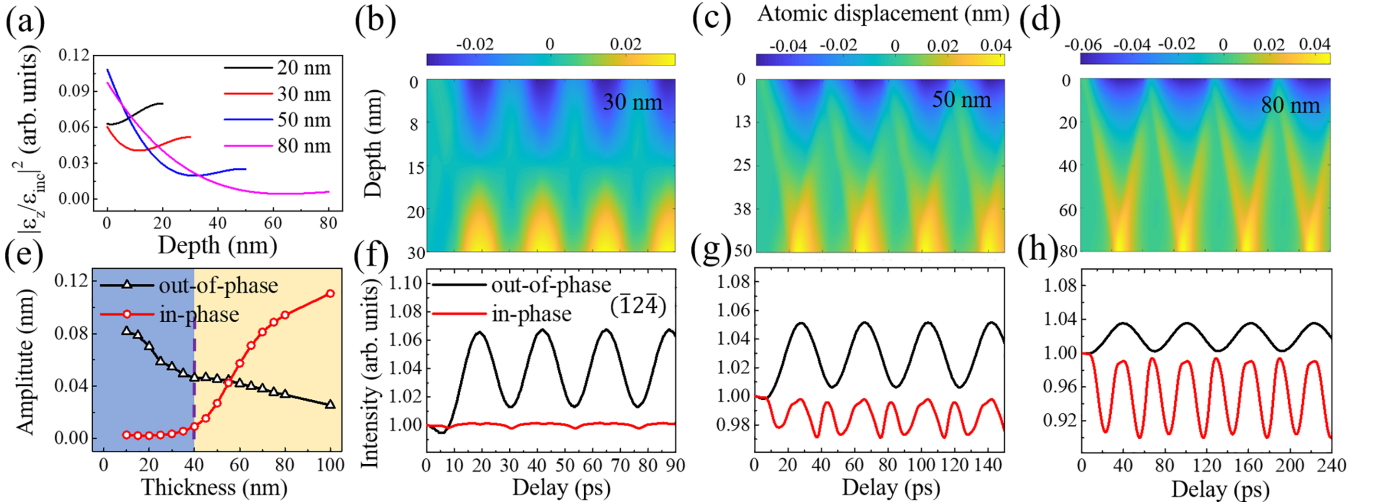


FIG. 3. Simulation of strain wave and kinematical diffraction intensity under varied thicknesses with laser fluence of 4.4 mJ/cm^2 . (a) Profile of depth-dependent electric field within samples with a thickness of 20, 30, 50, and 80 nm. (b)–(d) Dynamic simulation of depth-dependent atomic displacement with a sample thickness of 30, 50, and 80 nm, respectively. (e) Thickness-dependent amplitude of simulated intensity oscillations. (f)–(h) Kinematic simulation of intensity change of Bragg peak $(\bar{1}2\bar{4})$ with a sample thickness of 30, 50, and 80 nm, respectively. The total intensity is decomposed into in-phase and out of phase components.

change resulting from the Debye-Waller effect, which is directly related to the lattice temperature, can be evaluated using a single or double exponential function. As an approximation, we fit the intensity variation of peak (002) depicted in Fig. 1(e) to extract the temporal evolution of the lattice temperature [57]. This analysis yields a time constant of $\tau = 5.8 \pm 0.4 \text{ ps}$. Thus the lattice temperature can be expressed as follows:

$$T(z, t) = T(z)[1 - \exp(-t/\tau)], \quad (5)$$

where $T(z)$ represents the maximum lattice temperature attained after the electron-phonon coupling and Auger recombination processes. The value of $T(z)$ is dependent on the absorbed laser energy $E(z)$, which exhibits inhomogeneity along the depth z when the sample thickness is much greater than the optical penetration depth. The distribution of the maximum lattice carrier density after laser excitation is described by $n(z)$, which can be calculated using the laser energy distribution $E(z)$. The carrier density $n(z, t)$ takes the form

$$n(z, t) = g(t)n(z), \quad (6)$$

where $g(t)$ describes the carrier excitation and recombination processes. It is important to note that Eqs. (5) and (6) do not consider thermal diffusion and carrier diffusion, which is reasonable within a timescale of tens of picoseconds for transition metal dichalcogenides. Further information regarding the temporal evolution of thermoelasticity σ_T and deformation potential σ_e can be found in Supplemental Sec. S6 [40].

To calculate the distribution of absorbed laser energy $E(z)$, we solve the Maxwell equations with boundary conditions determined by the incidence geometry of the pump laser, following previous works [58,59]. Detailed calculations of $E(z)$, $T(z, t)$, and $n(z, t)$ can be found in the Supplemental Material [40] (Sec. S7). Figure 3(a) illustrates the calculated $|\frac{\epsilon_z}{\epsilon_{\text{inc}}}|^2$ in $2H\text{-MoTe}_2$ films with varying thicknesses. Here, ϵ_{inc} represents the incident electric field, and ϵ_z represents the electric field at depth z . This result demonstrates that as the

thickness increases, the inhomogeneity of the electric field inside the film becomes more pronounced.

We solve the elastodynamic wave equation using the finite difference method under these electric field profiles for thicknesses ranging from 10 to 80 nm. The initial and free boundary conditions are applied:

$$\begin{aligned} \mu(z, 0) &= 0, \\ \frac{\partial \mu}{\partial t} \Big|_{(z, 0)} &= 0, \\ \frac{\partial \mu}{\partial z} \Big|_{(0, t)} &= 0, \\ \frac{\partial \mu}{\partial z} \Big|_{(d, t)} &= 0. \end{aligned} \quad (7)$$

Figures 3(b)–3(d) display the calculated atomic displacements for each layer in 30, 50, and 80 nm films, respectively, with a laser fluence of 4.4 mJ/cm^2 . In the case of the 30 nm thickness, the sample is approximately homogeneously excited, leading to the dominant excitation of a typical standing wave. However, for the 50 nm thickness, in addition to the standing wave, a traveling wave propagating along the surface normal becomes evident. This traveling wave is even more pronounced in the 80 nm film.

V. APPEARANCE OF SECOND HARMONIC UNDER INHOMOGENEOUS EXCITATION

The inhomogeneous distribution of atomic displacements along the c direction gives rise to nonzero mean lattice constant difference $\bar{\Delta c} = \sum_i (\frac{\Delta c_i}{n_z})$ (Δc_i represents the change of lattice constant in the i th layer, and the standard deviation $S_c = \sqrt{\sum_i (\frac{(\Delta c_i - \bar{\Delta c})^2}{n_z}}$ becomes nonzero, where n_z is the total number of lattice layers in the film. In the simulations of diffraction intensity (kinematical diffraction calculation

considering the modulation of the acoustic wave; further details are described in the Supplemental Material, Sec. S3 [40]), the entire sample can be regarded as a superlattice, and the nonzero S_c reflects the disorder of atomic arrangements. An increase in S_c results in a decrease in the diffraction intensities of spots (hkl) with $l \neq 0$. To aid understanding, we describe the change in diffraction intensity using the classical reciprocal bar analogy. After laser excitation, the nonzero Δc causes the translation of the reciprocal bar along the reciprocal lattice vector \mathbf{c}^* , while the change in S_c decreases the overall amplitude of the reciprocal bar.

In the diffraction patterns along the zone axis, the initial deviation parameters s_z of the Friedel pairs both have positive values. Thus, the intensity oscillations caused by Δc and S_c exhibit in-phase and out of phase features, respectively. We calculated the mean lattice constant difference $\overline{\Delta c}$ and the standard deviation S_c for a 63 nm film, as shown in Supplemental Fig. S4(a) [40]. The mean difference $\overline{\Delta c}$ exhibits an oscillation with a frequency of 21 GHz, while the standard deviation S_c exhibits a 42 GHz oscillation. This indicates that the in-phase and out of phase oscillations observed in Fig. 2 stem from the position shift and intensity change of the reciprocal bars, respectively. The combination of these two factors gives rise to the complexity in the diffraction intensity oscillations. Supplemental Figs. S4(b)–S4(d) [40] provide schematics to aid in understanding the origin of the in-phase and out of phase oscillations.

The temporal evolution of the diffraction intensity of Bragg peaks can be obtained by introducing the time-dependent atomic motions shown in Figs. 3(b)–3(d) to the kinematic intensity Eq. (8):

$$I(s, t) = I_0(s, t) \exp[-4\pi^2 |\mathbf{K}|^2 (\langle \mu^2 \rangle_T - \langle \mu^2 \rangle_{T_0})], \quad (8)$$

where $\mathbf{K} = h\mathbf{a}^* + k\mathbf{b}^* + l\mathbf{c}^* + \mathbf{s}$, and \mathbf{s} is the deviation parameter. $I_0(s, t)$ is expressed as

$$I_0(s, t) \propto |A|^2 = \frac{\sin^2(\pi N_x \mathbf{K} \cdot \mathbf{a})}{\sin^2(\pi \mathbf{K} \cdot \mathbf{a})} \frac{\sin^2(\pi N_y \mathbf{K} \cdot \mathbf{b})}{\sin^2(\pi \mathbf{K} \cdot \mathbf{b})} \times \left| \sum_{n_z} F_{n_z} \exp[2\pi i \mathbf{K} \cdot (\mathbf{r}_n + \boldsymbol{\mu}_{n_z})] \right|^2. \quad (9)$$

Further details regarding the temporal intensity evolution of the Bragg peak ($\bar{1}2\bar{4}$) for sample thicknesses of 30, 50, and 80 nm can be found in Supplemental Sec. S5 [40]. The calculated temporal intensity evolution of the Bragg peak ($\bar{1}2\bar{4}$) for sample thicknesses of 30, 50, and 80 nm are individually shown in Figs. 3(f)–3(h), respectively. To examine the effect of thickness on coherent intensity oscillation, the calculated diffraction intensity can be decomposed into in-phase and out of phase components (see Supplemental Sec. S4 [40]: Mechanisms of in-phase and out of phase oscillation). The results reveal that out of phase oscillation dominates in thin films. However, as the thickness increases, the inhomogeneous excitation becomes more prominent, leading to more pronounced in-phase oscillations. The amplitudes of these two types of oscillations are plotted in Fig. 3(e), which displays a critical thickness of approximately 40 nm, indicating the occurrence of inhomogeneous excitation. This value is approximately equal to the thickness (42.6 nm in the case of

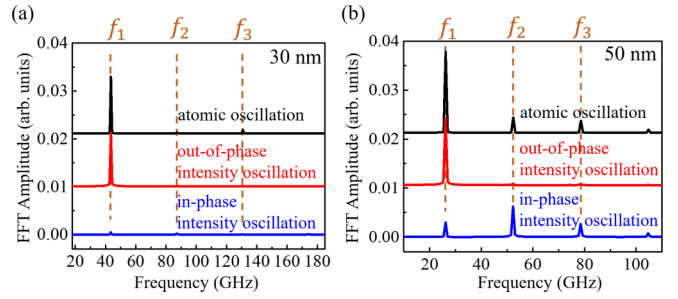


FIG. 4. Comparison of the frequencies of atomic displacement and intensity oscillation. Black line: FFT of the calculated atomic displacement at the top surface. Blue line: FFT of simulated out of phase intensity oscillation in Bragg peak ($\bar{1}2\bar{4}$). Red line: FFT of simulated in-phase intensity oscillation in Bragg peak ($\bar{1}2\bar{4}$). (a), (b) correspond to 30 and 50 nm film, respectively.

2H-MoTe₂, calculated by the absorption coefficient listed in Table S1 [40]) at which the laser energy density decays to $\frac{E_{inc}}{e^2}$ (where E_{inc} is the energy density of the incident laser, and e is Euler's number). These simulation results provide a satisfactory explanation for the experimentally observed in-phase and out of phase oscillations in the 27 and 63 nm films.

The oscillation frequency of the acoustic resonance mode satisfies $f_j = \frac{jv}{2d}$, ($j = 1, 2, 3, \dots$), representing acoustic phonons with different momentum. As previously reported [28,51], under homogeneous excitation, only the resonance modes with odd j values can be observed. However, under completely inhomogeneous excitation conditions, both even and odd resonance modes can be excited. The FFT of the simulated atomic displacement at the top surface of the film ($z = 0$) shown in Figs. 3(b) and 3(c) is represented by black lines in Figs. 4(a) and 4(b). The red and blue lines represent the FFT of the diffraction intensity oscillation shown in Figs. 3(f) and 3(g), respectively. In the case of homogeneous excitation in the 30 nm film, both the atomic motion and diffraction intensity primarily exhibit the fundamental oscillation with frequency f_1 , indicating that the fundamental oscillation of atomic positions does not contribute to the appearance of higher harmonics in the diffraction intensity. Therefore, the second harmonic observed in the in-phase oscillation [Fig. 4(b), 50 nm film] originates from the atomic oscillation with frequency f_2 . Comparing Figs. 3(a) and 4(b), it can be observed that the experimentally observed in-phase oscillation is a direct reflection of the higher harmonics induced by phonons with different momentum.

VI. AMPLIFICATION EFFECT ON THE SECOND HARMONIC OF WRINKLES

It has been mentioned that the initial boundary condition used in the calculation assumes $\mu(z, 0) = 0$. However, in materials obtained by mechanical exfoliation, this initial condition is inaccurate due to the presence of wrinkles. It has been previously reported that the presence of wrinkles can alter the structure and properties of the film [60]. To account for this, we introduce a simplified geometric configuration of wrinkles into the simulation. The left panel in Fig. 5(a) shows the geometric configuration, while the right panel provides a simplified schematic in which the wrinkle is approximated

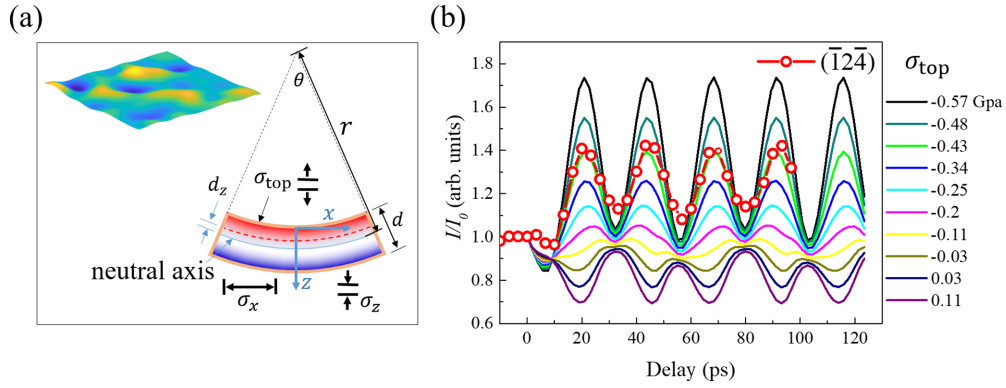


FIG. 5. Simulation of diffraction intensity oscillations in the presence of wrinkles. (a) Simplified geometric configuration of wrinkles. (b) Comparison of experimental data and diffraction simulation under varied strain σ_{top} . Red circles: experimentally measured intensity change of Bragg peak $(\bar{1}\bar{2}\bar{4})$. Solid lines: simulation results of $(\bar{1}\bar{2}\bar{4})$. σ_{top} denotes the out of plane longitudinal strain at the upper surface.

as an arc shape. In a bending film, in-plane compressive or tensile strain σ_x leads to an out of plane strain distribution σ_z . The strains at a distance d_z ($d_z = \frac{d}{2} - z$) from the neutral axis can be expressed as $\sigma_x = -C_{44}d_z/r$, $\sigma_z = -v\sigma_x = vC_{44}d_z/r$, where r represents the radius of the arc (depression: $r > 0$; bulge: $r < 0$) and v is the out of plane Poisson ratio. When a depression appears, the maximum out of plane compressive and tensile strains occur on the upper and lower surfaces, respectively. This wrinkle-induced longitudinal strain gradient results in a nonzero initial atomic displacement along the surface normal.

Given the relation $\sigma_z = C_{33} \frac{\partial \mu}{\partial z}$, the initial condition of $\mu(z, 0)$ can be expressed by the strain at the upper surface σ_{top} ($\sigma_{\text{top}} = v d C_{44} / 2r$),

$$\mu(z, 0) = -\frac{v C_{44} d_z^2}{2r C_{33}} = -\frac{\sigma_{\text{top}} d_z^2}{d C_{33}}. \quad (10)$$

We have solved wave Eq. (3) with the new initial condition in the 63 nm film and performed corresponding diffraction simulations of the Bragg peak $(\bar{1}\bar{2}\bar{4})$ using the calculated atomic motion. A comparison of the experimental and simulated results under varied strain (corresponding to different bending angles θ) is shown in Fig. 5(b). The positive and negative values of σ_{top} correspond to depression and bulge geometry, respectively. When $\sigma_{\text{top}} = -0.43$ GPa, the simulated and experimental results are essentially consistent. However, it should be noted that the actual geometry of the film is a complex combination of wrinkles with various shapes. Therefore, the simulation results in Fig. 5(b) only indicate that, on average, the film appears as a bulge. Stress due to the presence of wrinkles in the film breaks the symmetry of the crystallographic spacing distribution along the c direction, which enhances the response of the diffracted intensity to the second harmonic [Fig. 5(b)].

VII. CONCLUSION

In this study, we have investigated the inhomogeneous excitation of coherent longitudinal phonons in $2H\text{-MoTe}_2$ using ultrafast electron diffraction and electron diffraction simulations combined with finite element analysis. Our experimental results revealed the presence of high harmonics resulting from inhomogeneous excitation in thick samples.

We successfully decoupled the experimentally observed in-phase and out of phase oscillations of diffraction intensity to understand the effect of higher harmonics on the crystal structure. The out of phase signals, which represent homogeneous excitation, primarily exhibit the lowest-order coherent phonon modes and can be described as simple harmonic oscillations of the lattice constant c . We identified a critical thickness of approximately 40 nm, above which the effect of inhomogeneous excitation becomes increasingly pronounced. The induced higher harmonics, as reflected by the in-phase signals, indicate the presence of crystal disorder. Our analytical approach, incorporating the presence of wrinkles in the sample, allows for a clear correspondence between electron diffraction and coherent phonons. This provides valuable methodological guidance for studying nonequilibrium states and the structural modulation induced by acoustic phonons in inhomogeneous conditions.

ACKNOWLEDGMENTS

This work was supported by the National Key Research and Development Program of China (Grant No. 2021YFA1301502), the National Natural Science Foundation of China (Grants No. U22A6005 and No. 12074408), the Guangdong Major Scientific Research Project (Grant No. 2018KZDXM061), the Youth Innovation Promotion Association of CAS (Grant No. 2022004), the Scientific Instrument Developing Project of the Chinese Academy of Sciences (Grants No. YJKYYQ20200055, No. ZDKYYQ2017000, and No. 22017BA10), the Strategic Priority Research Program of the Chinese Academy of Sciences (Grants No. XDB25000000 and No. XDB33010100), Beijing Municipal Science and Technology Major Project No. Z201100001820006, the IOP Hundred Talents Program (Grant No. Y9K5051), the Postdoctoral Support Program of China (Grant No. 2020M670501), and the Synergetic Extreme Condition User Facility (SECUF).

The author contributions are as follows: Conceptualization: Y.Z., H.Y., Jun L. Methodology: Y.Z., S.S., Jun L. Investigation: Y.Z., W.W. Visualization: Y.Z., S.S., H.T. Instruction: Jianqi L., H.T., H.Y. The paper was written through contributions of all authors. All authors have given approval to the final version of the paper.

- [1] C. Giannetti, M. Capone, D. Fausti, M. Fabrizio, F. Parmigiani, and D. Mihailovic, Ultrafast optical spectroscopy of strongly correlated materials and high-temperature superconductors: A non-equilibrium approach, *Adv. Phys.* **65**, 58 (2016).
- [2] T. Dong, S. J. Zhang, and N. L. Wang, Recent development of ultrafast optical characterizations for quantum materials, *Adv. Mater.* **35**, 211068 (2022).
- [3] G. Huitric, M. Rodriguez-Fano, L. Gournay, N. Godin, M. Herve, G. Privault, J. Tranchant, Z. Khaldi, M. Cammarata, E. Collet, E. Janod, and C. Odin, Impact of the terahertz and optical pump penetration depths on generated strain waves temporal profiles in a V_2O_3 thin film, *Faraday Discuss.* **237**, 389 (2022).
- [4] H. Niwa, N. Yoshikawa, K. Tomari, R. Matsunaga, D. Song, H. Eisaki, and R. Shimano, Light-induced nonequilibrium response of the superconducting cuprate $La_{2-x}Sr_xCuO_4$, *Phys. Rev. B* **100**, 104507 (2019).
- [5] E. Mohr-Vorobeva, S. L. Johnson, P. Beaud, U. Staub, R. De Souza, C. Milne, G. Ingold, J. Demsar, H. Schaefer, and A. Titov, Nonthermal melting of a charge density wave in $TiSe_2$, *Phys. Rev. Lett.* **107**, 036403 (2011).
- [6] T. Huber, S. O. Mariager, A. Ferrer, H. Schaefer, J. A. Johnson, S. Grubel, A. Lubcke, L. Huber, T. Kubacka, C. Dornes, C. Laulhe, S. Ravy, G. Ingold, P. Beaud, J. Demsar, and S. L. Johnson, Coherent structural dynamics of a prototypical charge-density-wave-to-metal transition, *Phys. Rev. Lett.* **113**, 026401 (2014).
- [7] S. L. Johnson, P. Beaud, C. J. Milne, F. S. Krasniqi, E. S. Zijlstra, M. E. Garcia, M. Kaiser, D. Grolimund, R. Abela, and G. Ingold, Nanoscale depth-resolved coherent femtosecond motion in laser-excited bismuth, *Phys. Rev. Lett.* **100**, 155501 (2008).
- [8] S. Gerber, S. L. Yang, D. Zhu, H. Soifer, J. A. Sobota, S. Rebec, J. J. Lee, T. Jia, B. Moritz, C. Jia, A. Gauthier, Y. Li, D. Leuenberger, Y. Zhang, L. Chaix, W. Li, H. Jang, J. S. Lee, M. Yi, G. L. Dakovski *et al.*, Femtosecond electron-phonon lock-in by photoemission and x-ray free-electron laser, *Science* **357**, 71 (2017).
- [9] D. N. Basov, R. D. Averitt, and D. Hsieh, Towards properties on demand in quantum materials, *Nat. Mater.* **16**, 1077 (2017).
- [10] A. de la Torre, D. M. Kennes, M. Claassen, S. Gerber, J. W. McIver, and M. A. Sentef, Colloquium: Nonthermal pathways to ultrafast control in quantum materials, *Rev. Mod. Phys.* **93**, 041002 (2021).
- [11] M. Trigo, P. Giraldo-Gallo, J. N. Clark, M. E. Kozina, T. Henighan, M. P. Jiang, M. Chollet, I. R. Fisher, J. M. Glowia, T. Katayama, P. S. Kirchmann, D. Leuenberger, H. Liu, D. A. Reis, Z. X. Shen, and D. Zhu, Ultrafast formation of domain walls of a charge density wave in $SmTe_3$, *Phys. Rev. B* **103**, 054109 (2021).
- [12] S. F. Duan, Y. Cheng, W. Xia, Y. Y. Yang, C. Y. Xu, F. F. Qi, C. Z. Huang, T. W. Tang, Y. F. Guo, W. D. Luo, D. Qian, D. Xiang, J. Zhang, and W. T. Zhang, Optical manipulation of electronic dimensionality in a quantum material, *Nature (London)* **595**, 239 (2021).
- [13] M. Z. Hasan and C. L. Kane, Colloquium: Topological insulators, *Rev. Mod. Phys.* **82**, 3045 (2010).
- [14] A. A. Burkov, Topological semimetals, *Nat. Mater.* **15**, 1145 (2016).
- [15] S. Jia, S. Y. Xu, and M. Z. Hasan, Weyl semimetals, Fermi arcs and chiral anomalies, *Nat. Mater.* **15**, 1140 (2016).
- [16] X. F. Qian, J. W. Liu, L. Fu, and J. Li, Quantum spin Hall effect in two-dimensional transition metal dichalcogenides, *Science* **346**, 1344 (2014).
- [17] C. Thomsen, J. Strait, Z. Vardeny, H. J. Maris, J. Tauc, and J. J. Hauser, Coherent phonon generation and detection by picosecond light-pulses, *Phys. Rev. Lett.* **53**, 989 (1984).
- [18] C. Thomsen, H. T. Grahn, H. J. Maris, and J. Tauc, Surface generation and detection of phonons by picosecond light-pulses, *Phys. Rev. B* **34**, 4129 (1986).
- [19] A. M. Lindenberg, I. Kang, S. L. Johnson, T. Missalla, P. A. Heimann, Z. Chang, J. Larsson, P. H. Bucksbaum, H. C. Kapteyn, H. A. Padmore, R. W. Lee, J. S. Wark, and R. W. Falcone, Time-resolved x-ray diffraction from coherent phonons during a laser-induced phase transition, *Phys. Rev. Lett.* **84**, 111 (2000).
- [20] B. Barwick, H. S. Park, O. H. Kwon, J. S. Baskin, and A. H. Zewail, 4D imaging of transient structures and morphologies in ultrafast electron microscopy, *Science* **322**, 1227 (2008).
- [21] A. H. Zewail, Four-dimensional electron microscopy, *Science* **328**, 187 (2010).
- [22] A. Zong, A. Kogar, and N. Gedik, Unconventional light-induced states visualized by ultrafast electron diffraction and microscopy, *MRS Bull.* **46**, 720 (2021).
- [23] P. Ruello and V. E. Gusev, Physical mechanisms of coherent acoustic phonons generation by ultrafast laser action, *Ultrasonics* **56**, 21 (2015).
- [24] L. Dhar, J. A. Rogers, and K. A. Nelson, Time-resolved vibrational spectroscopy in the impulsive limit, *Chem. Rev.* **94**, 157 (1994).
- [25] T. Y. Jeong, B. M. Jin, S. H. Rhim, L. Debbichi, J. Park, Y. D. Jang, H. R. Lee, D. H. Chae, D. Lee, Y. H. Kim, S. Jung, and K. J. Yee, Coherent lattice vibrations in mono- and few-layer WSe_2 , *ACS Nano* **10**, 5560 (2016).
- [26] X. C. Miao, G. W. Zhang, F. J. Wang, H. G. Yan, and M. B. Ji, Layer-dependent ultrafast carrier and coherent phonon dynamics in black phosphorus, *Nano Lett.* **18**, 3053 (2018).
- [27] P. Soubelet, A. A. Reynoso, A. Fainstein, K. Nogajewski, M. Potemski, C. Faugeras, and A. E. Bruchhausen, The lifetime of interlayer breathing modes of few-layer $2H-MoSe_2$ membranes, *Nanoscale* **11**, 10446 (2019).
- [28] A. Nakamura, T. Shimojima, and K. Ishizaka, Finite-element simulation of photoinduced strain dynamics in silicon thin plates, *Struct Dyn.* **8**, 024103 (2021).
- [29] L. L. Wei, S. S. Sun, C. Guo, Z. W. Li, K. Sun, Y. Liu, W. J. Lu, Y. P. Sun, H. F. Tian, H. X. Yang, and J. Q. Li, Dynamic diffraction effects and coherent breathing oscillations in ultrafast electron diffraction in layered $1T-TaSeTe$, *Struct. Dyn.* **4**, 044012 (2017).
- [30] E. J. Sie, C. M. Nyby, C. D. Pemmaraju, S. J. Park, X. Z. Shen, J. Yang, M. C. Hoffmann, B. K. Ofori-Okai, R. K. Li, A. H. Reid, S. Weathersby, E. Mannebach, N. Finney, D. Rhodes, D. Chenet, A. Antony, L. Balicas, J. Hone, T. P. Devereaux, T. F. Heinz *et al.*, An ultrafast symmetry switch in a Weyl semimetal, *Nature (London)* **565**, 61 (2019).
- [31] R. A. Gnasbasik, P. K. Suri, J. L. Chen, and D. J. Flannigan, Imaging coherent phonons and precursor dynamics in $LaFeAsO$

- with 4D ultrafast electron microscopy, *Phys. Rev. Mater.* **6**, 024802 (2022).
- [32] A. Nakamura, T. Shimojima, Y. Chiashi, M. Kamitani, H. Sakai, S. Ishiwata, H. Li, and K. Ishizaka, Nanoscale imaging of unusual photoacoustic waves in thin flake VTe₂, *Nano Lett.* **20**, 4932 (2020).
- [33] A. Feist, N. R. da Silva, W. X. Liang, C. Ropers, and S. Schafer, Nanoscale diffractive probing of strain dynamics in ultrafast transmission electron microscopy, *Struct. Dyn.* **5**, 014302 (2018).
- [34] W. X. Liang, G. M. Vanacore, and A. H. Zewail, Observing (non)linear lattice dynamics in graphite by ultrafast Kikuchi diffraction, *Proc. Natl Acad. Sci. USA* **111**, 5491 (2014).
- [35] H. Zhu, Q. X. Wang, L. X. Cheng, R. Addou, J. Y. Kim, M. J. Kim, and R. M. Wallace, Defects and surface structural stability of MoTe₂ under vacuum annealing, *ACS Nano* **11**, 11005 (2017).
- [36] S. Song, D. H. Keum, S. Cho, D. Perello, Y. Kim, and Y. H. Lee, Room temperature semiconductor-metal transition of MoTe₂ thin films engineered by strain, *Nano Lett.* **16**, 188 (2016).
- [37] F. Zhang, H. R. Zhang, S. Krylyuk, C. A. Milligan, Y. Q. Zhu, D. Y. Zemlyanov, L. A. Bendersky, B. P. Burton, A. V. Davydov, and J. Appenzeller, Electric-field induced structural transition in vertical MoTe₂- and Mo_{1-x}W_xTe₂-based resistive memories, *Nat. Mater.* **18**, 55 (2019).
- [38] Q. Gu, A. Falk, J. Q. Wu, O. Y. Lian, and H. Park, Current-driven phase oscillation and domain-wall propagation in W_xV_{1-x}O₂ nanobeams, *Nano Lett.* **7**, 363 (2007).
- [39] E. Strelcov, Y. Lilach, and A. Kolmakov, Gas sensor based on metal-insulator transition in VO₂ nanowire thermistor, *Nano Lett.* **9**, 2322 (2009).
- [40] See Supplemental Material at <http://link.aps.org/supplemental/10.1103/PhysRevB.108.245426> for the determination of sample thickness, more details about the specimen and the simulation of electron diffraction, details about the calculation of stress, and the determination of laser excitation profiles. It also contains Refs. [41–45].
- [41] T. Malis, S. C. Cheng, and R. F. Egerton, EELS log-ratio technique for specimen-thickness measurement in the TEM, *J. Electron Microsc. Tech.* **8**, 193 (1988).
- [42] A. Krishnamoorthy, M. F. Lin, X. Zhang, C. Weninger, R. R. Ma, A. Britz, C. S. Tiwary, V. Kochat, A. Apte, J. Yang, S. Park, R. K. Li, X. Z. Shen, X. J. Wang, R. Kalia, A. Nakano, F. Shimojo, D. Fritz, U. Bergmann, P. Ajayan *et al.*, Optical control of non-equilibrium phonon dynamics, *Nano Lett.* **19**, 4981 (2019).
- [43] A. J. Grant, T. M. Griffiths, G. D. Pitt, and A. D. Yoffe, Electrical properties and magnitude of indirect gap in semiconducting transition-metal dichalcogenide layer crystals, *J. Phys. C: Solid State Phys.* **8**, L17 (1975).
- [44] S. H. Elmahalawy and B. L. Evans, Thermal-expansion of 2H-MoS₂, 2H-MoSe₂ and 2H-WSe₂ between 20 and 800 °C, *J. Appl. Crystallogr.* **9**, 403 (1976).
- [45] A. R. Beal and H. P. Hughes, Kramers-Kronig analysis of the reflectivity spectra of 2H-MoS₂, 2H-MoSe₂ and 2H-MoTe₂, *J. Phys. C: Solid State Phys.* **12**, 881 (1979).
- [46] W. G. Dawson and D. W. Bullett, Electronic-structure and crystallography of MoTe₂ and WTe₂, *J. Phys. C: Solid State Phys.* **20**, 6159 (1987).
- [47] D. H. Keum, S. Cho, J. H. Kim, D. H. Choe, H. J. Sung, M. Kan, H. Kang, J. Y. Hwang, S. W. Kim, H. Yang, K. J. Chang, and Y. H. Lee, Bandgap opening in few-layered monoclinic MoTe₂, *Nat. Phys.* **11**, 482 (2015).
- [48] C. Ruppert, O. B. Aslan, and T. F. Heinz, Optical properties and band gap of single- and few-layer MoTe₂ crystals, *Nano Lett.* **14**, 6231 (2014).
- [49] D. B. Sirdeshmukh, L. Sirdeshmukh, and K. G. Subhadra, *Micro- and Macro-Properties of Solids* (Springer, Berlin, 2006).
- [50] E. Stellino, F. Capitani, F. Ripanti, M. Verseils, C. Petrillo, P. Dore, and P. Postorino, Broadband infrared study of pressure-tunable Fano resonance and metallization transition in 2H-MoTe₂, *Sci. Rep.* **12**, 17333 (2022).
- [51] Q. K. Qian, X. Z. Shen, D. Luo, L. X. Jia, M. Kozina, R. K. Li, M. F. Lin, A. H. Reid, S. Weathersby, S. Park, J. Yang, Y. Zhou, K. Y. Zhang, X. J. Wang, and S. X. Huang, Coherent lattice wobbling and out-of-phase intensity oscillations of Friedel pairs observed by ultrafast electron diffraction, *ACS Nano* **14**, 8449 (2020).
- [52] L. Liang, J. Zhang, B. G. Sumpter, Q.-H. Tan, P.-H. Tan, and V. Meunier, Low-frequency shear and layer-breathing modes in Raman scattering of two-dimensional materials, *ACS Nano* **11**, 11777 (2017).
- [53] G. Froehlicher, E. Lorchat, F. Fernique, C. Joshi, A. Molina-Sanchez, L. Wirtz, and S. Berciaud, Unified description of the optical phonon modes in *N*-layer MoTe₂, *Nano Lett.* **15**, 6481 (2015).
- [54] A. Nakamura, T. Shimojima, M. Matsuura, Y. Chiashi, M. Kamitani, H. Sakai, S. Ishiwata, H. Li, A. Oshiyama, and K. Ishizaka, Evaluation of photo-induced shear strain in monoclinic VTe₂ by ultrafast electron diffraction, *Appl. Phys. Express* **11**, 092601 (2018).
- [55] J.-H. Kim, M. R. Bergren, J. C. Park, S. Adhikari, M. Lorke, T. Frauenheim, D.-H. Choe, B. Kim, H. Choi, T. Gregorkiewicz, and Y. H. Lee, Carrier multiplication in van der Waals layered transition metal dichalcogenides, *Nat. Commun.* **10**, 5488 (2019).
- [56] Z. Chi, H. Chen, Q. Zhao, and Y.-X. Weng, Ultrafast carrier and phonon dynamics in few-layer 2H-MoTe₂, *J. Chem. Phys.* **151**, 114704 (2019).
- [57] O. B. Wright and V. E. Gusev, Acoustic generation in crystalline silicon with femtosecond optical pulses, *Appl. Phys. Lett.* **66**, 1190 (1995).
- [58] M. Milosevic and S. L. Berets, Applications of the theory of optical spectroscopy to numerical simulations, *Appl. Spectrosc.* **47**, 566 (1993).
- [59] S. W. King and M. Milosevic, A method to extract absorption coefficient of thin films from transmission spectra of the films on thick substrates, *J. Appl. Phys.* **111**, 073109 (2012).
- [60] D. Du, S. Manzo, C. Zhang, V. Saraswat, K. T. Genser, K. M. Rabe, P. M. Voyles, M. S. Arnold, and J. K. Kawasaki, Epitaxy, exfoliation, and strain-induced magnetism in rippled Heusler membranes, *Nat. Commun.* **12**, 2494 (2021).